ISIJ International, Vol. 63 (2023), No. 3, pp. 407–418
https://doi.org/10.2355/isijinternational.ISIJINT-2022-408

Review

Current Status and Future Scope of Phase Diagram Studies

Masanori ENOKI,[1)]* Satoshi MINAMOTO,[2)] Ikuo OHNUMA,[2)] Taichi ABE[2)] and Hiroshi OHTANI[3)]

1) Institute of Multidisciplinary Research for Advanced Materials, Tohoku University, Sendai, 980-8577 Japan.
2) National Institute for Materials Science, 1-2-1 Sengen, Tsukuba, Ibaraki, 305-0047 Japan.
3) Toyota Physical and Chemical Research Institute, 41-1, Yokomichi, Nagakute, Aichi, 480-1192 Japan.

(*Received on September 21, 2022; accepted on November 24, 2022*)

Research on alloy phase diagrams started in the middle of the 19th century and progressed into the laborious and time-consuming process of constructing phase diagrams through experiments and phenomenological calculations with thermodynamic analysis. More recently, phase diagram research has evolved into the computation of theoretical phase diagrams based on first-principles calculations and the development of new materials for high-throughput data-driven types of phase diagrams. This paper discusses the features and problems of each technique using a collection of recent papers, with the aim of describing future problems in this field.

KEY WORDS: diffusion couple; CALPHAD method; thermodynamic analysis; first-principles calculations; data-driven approach.

1. Introduction

The phase diagram plays a very important role in controlling the functionalities of various materials. Rudberg's 1830 investigation of the Sn–Bi binary phase diagrams may be one of the oldest articles on alloy phase diagrams. Because of the limitations of the temperature measurement method at the time, these studies were limited to low-melting-point alloys, but the development of a Pt Pt–Rh thermocouple by Le Chatelier enabled high-temperature measurements, and Roberts–Austen used this thermocouple to study the Fe–C phase diagram. Since roughly 1970, the calculation of phase diagrams (CALPHAD) method illustrated in this paper has been in use, and the field of phase diagram studies has been pursued to date. In recent years, various theoretical calculations and data science techniques representing first-principles calculations have been applied to practical alloys, and the concept of computational thermodynamics has broadened in scope. This work aims to cover not only the experimental and CALPHAD methods but also a new phase diagram study based on electronic theory calculation and data scientific method as widely as possible.

This paper is structured as follows. After this introductory text, Section 2 explains the experimental techniques used in phase diagram determination, particularly new experimental methods that can determine the equilibria of low-temperature and multicomponent systems, which have been previously considered difficult to determine experimentally. The thermodynamic models and databases used in the CALPHAD method, as well as various software packages, are introduced in Section 3. The free energy at finite temperatures of solid solutions, liquids, and compounds calculated by the technique based on first-principles calculations is presented in Section 4, together with the computational techniques of theoretical phase diagrams and the ground-state search. The technique of predicting thermodynamic physical properties of the data-driven type, which is also being applied in the field of material development using machine learning and AI technologies, and an actual example is demonstrated in Section 5.

2. Experimental Determination of Phase Diagrams

It is widely known that phase diagrams of multicomponent systems can be determined using a wide variety of advanced equipment. Transformation temperatures, equilibrium compositions, and crystal structures of equilibrium phases are measured and analyzed using thermal analysis, microstructure examination, chemical composition measurements, and X-ray or electron diffraction analysis. Such methods for determining phase diagrams have been reviewed in detail in the literature.[1)] This section focuses not on experimental equipment methods but on the preparation of equilibrated samples of multicomponent alloys for effective phase diagram determination under difficult conditions of low temperature[2)] and on the high-throughput diffusion multiple (DM) method.[3)]

* Corresponding author: E-mail: enoki@tohoku.ac.jp

2.1. Experimental Procedure and Results for Low-temperature Phase Equilibrium Determination

Induction melting of electrolytic Fe (99.99%) and electrolytic Ni (99.99%) under an Ar atmosphere produced Fe–Ni binary alloys; these were powdered by the gas-atomizing method using high-purity Ar. The powder was placed in a stainless-steel chamber with high-carbon Cr steel balls that were rotated together, struck by a guide vane, hurled into an impact area, and crashed into the chamber wall (**Fig. 1**(a)). A portion of the powder was severely deformed, whereas the rest maintained its spherical shape without deformation (Figs. 1(b) and 1(c), respectively). Each converge-milled powder was sealed in an evacuated quartz capsule and heat-treated for equilibration between 400 and 700°C. A field emission-electron probe micro analysis (FE-EPMA: JEOL JXA-8500F) with a 20 kV accelerating voltage was used to examine the microstructure of the as-atomized and heat-treated samples. The equilibrium compositions of the powder particles exhibiting two-phase microstructure after the heat treatment were determined by FE-EPMA with an accelerating voltage of 6 kV, a condition at which the spatial resolution of the microprobe analysis can be controlled below approximately 0.5 μm.

Figures 1(b) and 1(c) present the backscattered electron (BSE) images of a severely deformed and an undeformed particle of the Fe–11.5 at.%Ni alloy, respectively, equilibrated at 500°C. The former microstructure was formed by recrystallization of a severely deformed martensite structure (α'_d), resulting in the formation of equiaxed α-bcc (dark) and γ-fcc (bright) dual-phase grains, whereas the latter was formed by precipitation of γ-fcc particles aligned in the annealed α' martensite (α'_a) matrix, consisting of supersaturated Ni in α'-Fe. The equilibrium state of severely deformed particles could be achieved in recrystallized dual-phase microstructure heat-treated for 283 d at 400°C. This temperature (400°C) is significantly lower than half of the melting temperature of Fe ($T_m^{Fe}/2 \fallingdotseq 900$ K $\fallingdotseq$ 630°C, $T_m^{Fe} = 1\,811$ K), below which neither long-range diffusion of Fe and Ni nor the equilibration of Fe–Ni alloys can occur. It was also confirmed that the equilibrium state for the γ-precipitation (γ_p) in an undeformed α' martensite matrix cannot be achieved below 600°C. Thus, it was concluded that severe deformation prior to equilibration is an effective way of decreasing the heat-treatment temperature by approximately 20% compared with conventional equilibration, enabling phase diagram determination at low temperature.

The experimental results are summarized in **Fig. 2**(a), and a thermodynamic assessment was carried out based

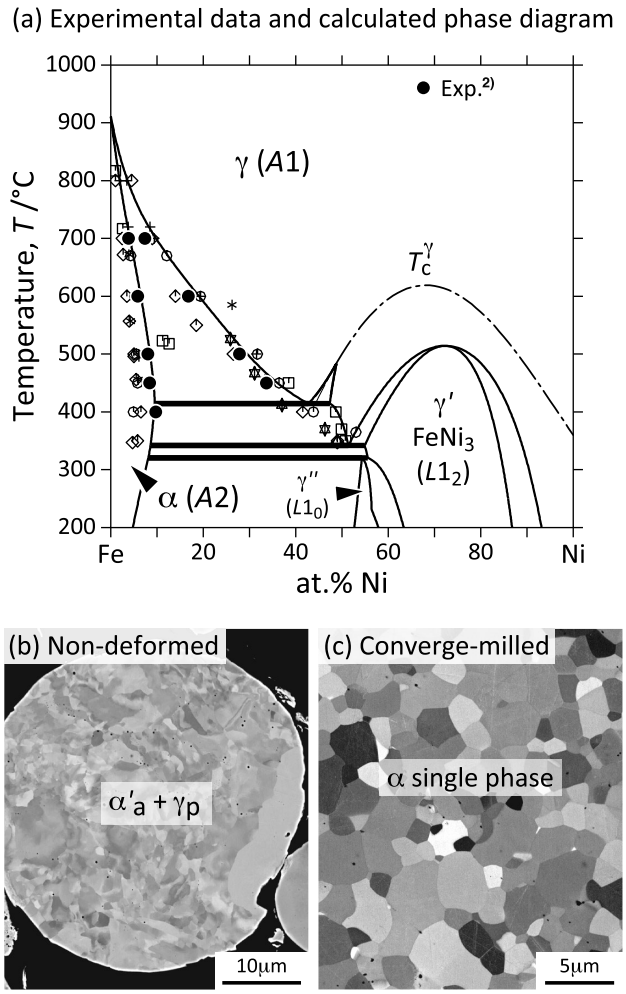

Fig. 2. (a) Summary of experimental results of α/γ equilibrium.[2] Calculated phase diagrams with revised thermodynamic parameters are superimposed. Results of FE-EPMA mapping analysis on (b) undeformed[2] and (c) deformed particles of a Fe–7.6 at.%Ni alloy heat-treated at 500°C for 143 days.

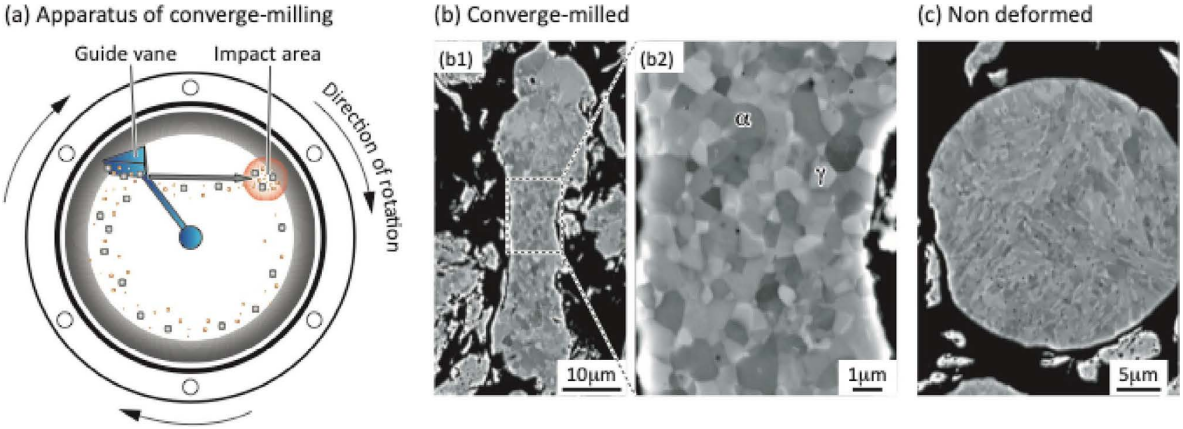

Fig. 1. (a) Apparatus for the converge-milling process;[2] BSE images of microstructure of (b) converge-milled (at two different magnifications) and (c) particle of Fe–11.5 at.%Ni alloy without converge-milling heat-treated at 500°C for 2 months. (Online version in color.)

on them. The Ni solubility in the α-Fe phase increased according to the revised phase diagram, compared with the reported data, which was confirmed by the evidence shown in Figs. 2(b) and 2(c). An undeformed particle of the Fe–7.6 at.%Ni alloy heat-treated at 500°C for 143 d exhibited γ_p + α'_a dual-phase microstructure, whereas a severely deformed particle under the same conditions exhibited single α phase microstructure. The former and latter results are consistent with the previous and current solubility curves, respectively. Low-temperature phase diagrams are also expected to be determined by other severe deformation processes, such as high-pressure torsion.

2.2. Experimental Procedure and Results for Determination of a High-throughput Phase Diagram by Diffusion Multiple[3)]

Cubic samples of pure Ni (99.9%) and Mn (99.9%) were prepared, and the Mn cuboid was melted in an induction furnace on top of the Ni cuboid to fabricate a Ni/Mn diffusion couple (DC), which was then diffusion annealed at 1 000°C for 168 h to obtain a Ni–Mn composition gradient zone. Next, near the diffusion zone of the Ni/Mn DC, a cylindrical 3 mm diameter hole was formed, and In (99.99%) chips were inserted into the hole. Diffusion triples (DTs) were finally obtained by diffusion annealing for 3, 12, or 24 h in evacuated quartz tubes at 850°C above the melting temperature of In (156.6°C). The obtained DTs were cut along an In cylinder center line perpendicular to the Ni/Mn interface, the surfaces of which were polished and chemically analyzed using an EPMA along some lines parallel to the Ni/Mn interface. The line studies along the diffusion pathways produced information on phase equilibria over a wide composition range. Some Ni–Mn–In alloys were prepared and equilibrated, their microstructure was examined, and their chemistry was analyzed to confirm and supplement the equilibrium data acquired by DTs.

In addition to the so-called phase equilibrium determination, the DTs were used to determine the iso-M_S and iso-T_C curves in a combinatory manner, where M_S and T_C represent the martensitic transformation start temperature and the Curie temperature, respectively. In the Ni–Mn–In system, the $\beta(B2)$ phase at high temperatures transforms to martensite β(M) at certain temperatures during cooling, depending on its chemical composition. Some of the $\beta(B2)$ phase regions in the composition gradient DTs transformed to β(M) martensite at room temperature (RT) after quenching from high temperatures, whereas the other regions remained as the $\beta(B2)$ phase. The chemical compositions measured along the β(M)/$\beta(B2)$ pseudo-boundaries then correspond to the iso-M_S curve at RT. The iso-T_C curve at RT in the $\beta(B2)$ phase can also be determined from the chemical compositions measured along the ferro-/nonmagnetic pseudo-boundary in the composition gradient DTs. A magnetic colloidal solution was spread on the DT surface to make the pseudo-boundary show where the magnetic constituents in the solution segregated on the leakage field from the magnetic domain boundary in the ferromagnetic phase and darkened the brightness of ferromagnetic regions.

The microstructure in the vicinity of the diffusion zone of a DT sample heat-treated at 850°C is shown in **Fig. 3**(a). Three distinct regions, *i.e.*, the Ni-rich $\gamma(A1)$, the Mn-rich $\gamma(A1)$, and the In-rich $\beta(B2)$ phases, are observed on the left, lower right, and center, respectively. Two other regions were recognized, β(M) martensite with lamella-like morphology and another that was a liquid phase at 850°C and solidified as (In) at RT. The equilibrium compositions of the observed phases were determined by various concentration–penetration profiles across two phases measured by EPMA for a DT sample. An isothermal phase diagram of the Ni–Mn–In system at 850°C determined using the DT sample and equilibrated ternary alloys is shown in Fig. 3(b). Except for liquid/Mn_3In and Mn_3In/β-Mn, most two-phase equilibria were determined from a single DT sample (Fig. 3(b)). For the reason above, the DT method is referred to as a high-throughput technique for phase diagram determination. Other two-phase equilibria and three-phase triangles that could not be determined using the DT method were determined using two- or three-phase equilibrated alloys.

In the DM method, the stable intermediate phases may not form or be recognized due to very small interdiffusion

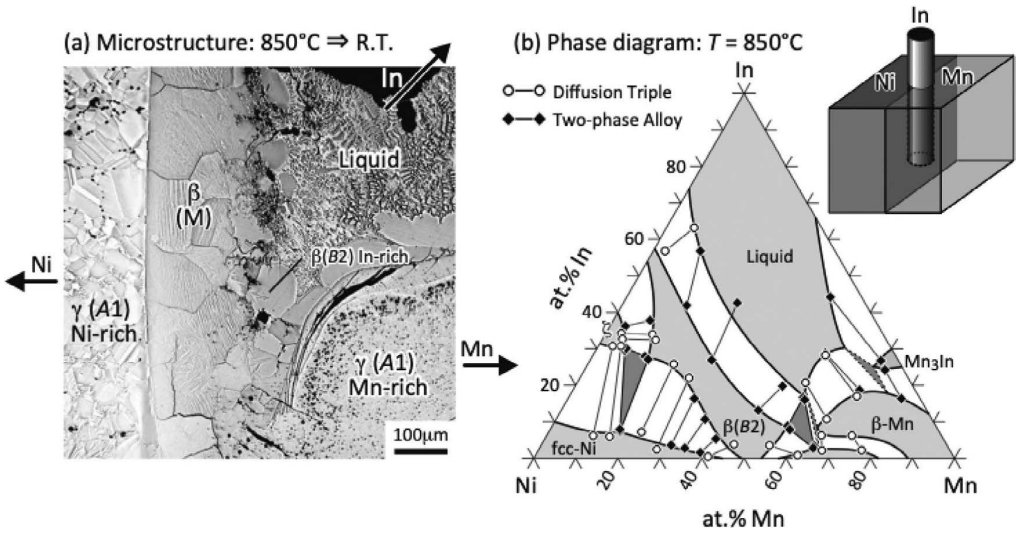

Fig. 3. (a) Microstructure in the vicinity of the diffusion zone in the DT annealed at 850°C.[3)] "M" indicates the partially formed martensite region in the $\beta(B2)$ phase region during cooling from the annealing temperature. (b) Phase equilibria of the Ni–Mn–In ternary system at 850°C determined with DTs and alloy specimens.[3)]

coefficients of constituent elements in these phases and also due to unsuitable diffusion paths avoiding the chemical concentration range of these phases in ternary or higher-order systems. Consequently, the existence of the stable phases could be missed, which should be taken into account when performing experiments using DM samples. By contrast, new stable phases that have not been reported previously could be discovered in DM samples, in which the Mn_3Ni_2In compound phase was found for the first time in the Ni–Mn–In system at 700°C.[3] Therefore, it should be always kept in mind that the DM method has both advantages and disadvantages.

Local equilibrium is not always fulfilled at a migrating interface caused by the interface reaction in DM samples, because the driving energy, which is compensated for the interface migration, causes deviation of the common tangent relationship, *i.e.*, the equilibrium condition, between the Gibbs energies of the two phases across the interface. Such an unfavorable discrepancy can be recognized in two-phase equilibria determined from the equilibrated alloys and the DM samples (Fig. 3(b)). Therefore, double checks using multiphase equilibrated alloys are indispensable in determining phase diagrams by the DM method.

The microstructure of the $\beta(B2)$ phase of the DT sample heat-treated at 850°C and quenched in iced water is shown in **Fig. 4**(a). It consisted of the β(M) martensite and the β(P) parent phase at RT. A dashed line denotes the clearly recognized pseudo-boundary between two regions. EPMA was used to analyze the chemical composition along the line, and the β(M)/β(P) boundary, which corresponds to the iso-M_S curve at RT, was determined as shown in Fig. 4(d). An optical microscope image of the $\beta(B2)$ phase in the same sample mentioned above is shown in Fig. 4(b). The magnetic constituents in the colloidal solution were segregated on the ferromagnetic region (Fig. 4(b)), and the chemical composition is plotted along a dashed line in Fig. 4(c). The both ends of the ferromagnetic domain and the boundary compositions are determined in Figs. 4(b) and 4(c), respectively. Chained curves were used to draw the pseudo-boundaries between the ferro- and nonmagnetic regions of the $\beta(B2)$ phase at 20°C in Fig. 4(d). The boundary of low In content almost coincides with the iso-M_S curve in Fig. 4(d) because the ferromagnetism in the $\beta(B2)$ phase was lost in the β(M) martensite. Finally, it is suggested that the combinatorial determination of phase diagrams at 850°C including iso-M_S and iso-T_C curves at RT can be realized effectively using a high-throughput technique, such as DM samples. Ideally, one isothermal section phase diagram can be determined from a single equilibrated DM sample, but in fact equilibrated multicomponent alloys should be examined to confirm and supplement the lack of experimental data.

3. The CALPHAD Method

Investigations on alloy phase diagrams began in the early years of the 19th century; at present, the mostly examined phase diagrams are those of unary, binary, and ternary systems. However, for practical alloy systems, which consist of many elements, it is difficult to obtain all the necessary phase equilibria only from experiments because this would require a large number of experiments. To overcome this difficulty, the CALPHAD approach was proposed, in which existing experimental data are analyzed using thermodynamic models, and phase diagrams and thermodynamic quantities are calculated and assessed with computers.[4–7)]

3.1. Thermodynamic Models

3.1.1. Thermodynamic Models for Condensed Phases

For solution phases, the regular solution model[8,9)] is used in the CALPHAD-type assessments. The Gibbs energy of a solution phase, ϕ, is expressed as the sum of four terms (Eq. (1)):

$$G_m^{\phi} = \sum x_i {}^0G_i + RT\sum x_i \ln x_i + {}^{ex}G_m^{Bin} + {}^{ex}G_m^{Ter} \ \left[\mathrm{J/mol}\right], \quad \ldots\ldots (1)$$

where G_m^{ϕ} is molar Gibbs energy of ϕ phase, R is gas constant, T is the absolute temperature, and x_i is the mole fraction of element i. The first term on the right-hand side of Eq. (1) is the molar Gibbs energy for the pure elements. This is called the lattice stability and is provided as the Scientific Group Thermodata Europe (SGTE)–Pure database.[10,11)] The second term is the molar Gibbs energy attributed to the con-

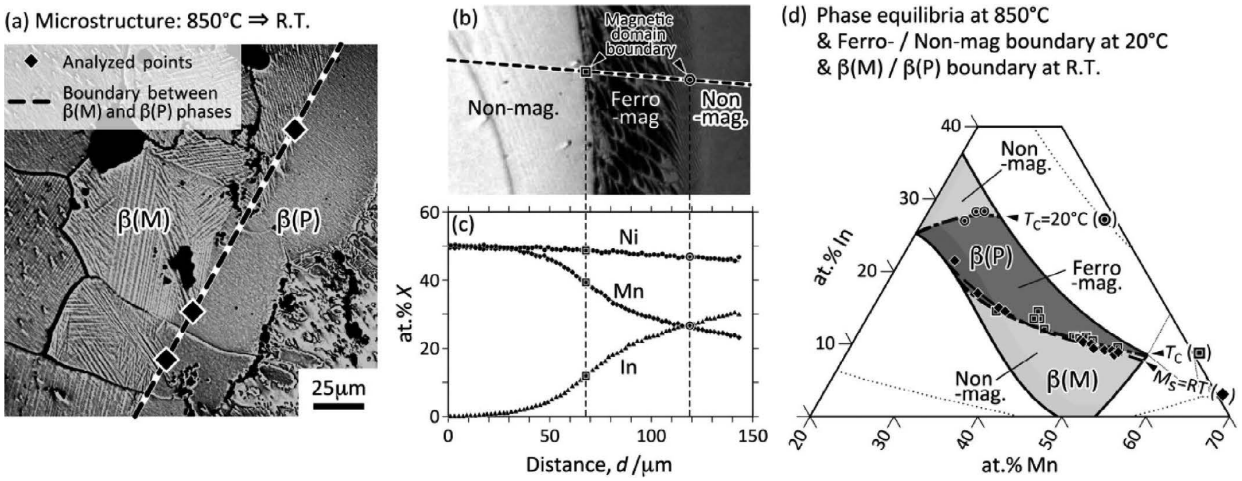

Fig. 4. Microstructure in the vicinity of the β phase (a) including the pseudo-boundary between the martensite "M" and parent "P" phase regions[3)] and (b) covered with magnetic colloid in the DT,[3)] (c) chemical composition analysis along the line indicated in (b), and (d) existing region of ferromagnetic/martensite phases at RT.

figuration entropy[12] with point probability. The third term is the binary excess Gibbs energy, given by the Redlich–Kister polynomial.[13] For an A–B binary solution, it is given by

$$ {}^{ex}G_m^{Bin} = x_A x_B \sum_{n=0}^{v} {}^{(n)}L_{A,B}(x_A - x_B)^n \ \left[\mathrm{J/mol}\right], \quad \ldots\ldots (2) $$

where ${}^{(n)}L_{A,B}$ is the interaction parameter between elements A and B. The fourth term is the ternary excess Gibbs energy[14] given by

$$ {}^{ex}G_m^{Ter} = x_A x_B x_C \left(x_A \, {}^{(1)}L_{A,B,C} + x_B \, {}^{(2)}L_{A,B,C} + x_C \, {}^{(3)}L_{A,B,C} \right) \left[\mathrm{J/mol}\right], \quad \ldots\ldots (3) $$

where ${}^{(n)}L_{A,B,C}$ is the ternary interaction parameter of elements A, B, and C. These interaction parameters are temperature dependent and in thermodynamic assessments are optimized to experimental and theoretical data.

The sublattice model[15,16] is introduced to describe the long-range ordering of compounds and interstitial atoms in solid solutions. For the liquid phase, several models are proposed: the quasi-chemical model[17] and the associate solution model[18] for liquids with the short-range ordering (SRO), the two-sublattice ionic solution model[19] for ionic liquids, and the Flory–Huggins model[20,21] for polymers.

The cluster variation method (CVM)[22] was used for more accurate descriptions of the configurational entropy than the point probability in Eq. (1) and SRO in solids. The Fe–Ni binary phase diagram in **Fig. 5**[23] is an example of a phase diagram calculated based on the CVM with the octahedral–tetrahedral approximation. Although the CVM is a precise model for representing atomic configurations, for expansions to higher-order systems and practical alloy systems, it requires fitting of a large number of parameters. Although it is limited to the weak SRO, formalism of the effect of SRO within the framework of the CALPHAD has been proposed a formulation of the effect of SRO based on the sublattice models in an FCC phase,[24,25] a BCC phase,[26] and FCC/BCC phases in high entropy alloys.[27]

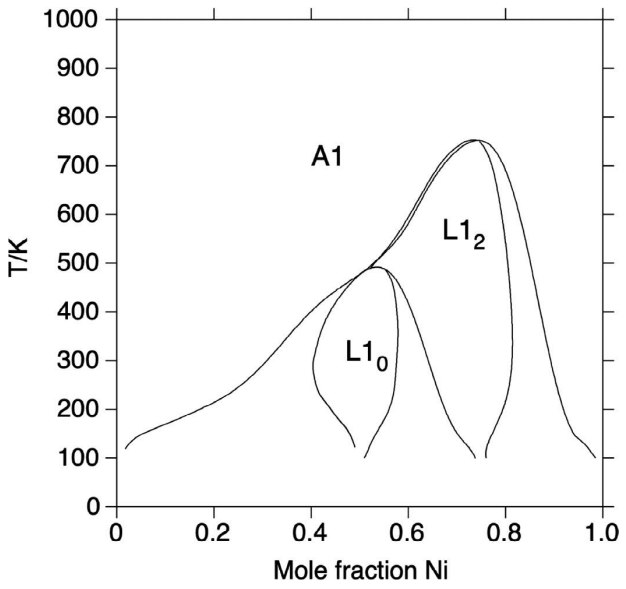

Fig. 5. Theoretical phase diagram of the Fe–Ni binary system based on the cluster variation method with the tetrahedron–octahedron approximation.[23]

3.1.2. Thermodynamic Models for Phase Transitions and Crystal Defects

For magnetic transitions, Inden[28] proposed a second-order transition model where the temperature dependency of the excess heat capacity was described by a logarithmic term. Hillert and Jarl[29] simplified the Inden model by applying a polynomial expansion to the logarithmic term. This modified Inden model is widely accepted in CALPHAD-type assessments. The magnetic-excess specific heats calculated from the two models are presented in **Fig. 6**, where the two curves are in good agreement except in the vicinity of the transition point at $\tau = 1$. Further modifications of the Inden model have been proposed by Chen and Sundman[30] and Xiong *et al.*[31]

For crystal defects, the Gibbs energies of the phases with mono- and di-vacancies have been proposed.[32–34] In a dilute solution, a description of monovacancy–solute atom pairs has been formulated using ternary interaction parameters.[34] Although dislocations are important lattice defects, they have not been formulated yet. The Inden model can be applied for the glass transitions[35] as it is appropriate to describe the second-order transition. The Inden model has a sharp peak at the transition temperature, but for the glass transitions a broad peak is observed (Fig. 6). Therefore, the Inden model should be carefully applied to transitions.

In the future, the metal–insulator transition and the superconducting transition will have to be modeled in the framework of the CALPHAD method, because the third-generation lattice stability reaches extremely low temperatures. Moreover, to enrich the Gibbs energy expressions, the pressure dependency of the Gibbs energy[36] needs to be included in the thermodynamic databases as well as other property data such as viscosity, diffusion coefficient, thermal conductivity, and thermal expansion coefficient.

3.2. Thermodynamic Software Packages

Table 1 lists the thermodynamic software packages.[37–44] Although many of these are commercial software packages, open-source codes, OpenCALPHAD[43] and PyCALPHAD,[44]

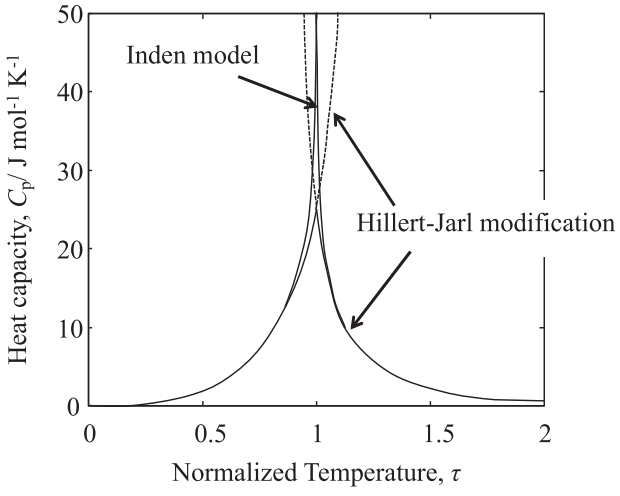

Fig. 6. Magnetic excess heat capacity, C_P, given by the Inden model[28] and the Hillert–Jarl modification,[29] where τ is the temperature normalized by the Curie temperature.

Table 1. Available thermodynamic software packages.

Program	Vender or Developer	Ref.
CaTCalc	AIST	37)
Malt2	MALT group	38)
PANDAT	CompTherm	39)
FactSage	CRCT/GTT	40)
DICTRA	Thermo-Calc AB	41)
Thermo-Calc	Thermo-Calc AB	41)
Lukas Program	H. L. Lukas	42)
PyCALPHAD	R. Otis	44)
OpenCalphad	B. Sundman	43)

are also available. These open-source codes provide the flexibility of introducing your thermodynamic model into the package, of including the packages in your code, and of easily modifying the parameters of the thermodynamic models in the package.

The phase diagram calculations can be used as a source of high-throughput thermodynamic data.[45–47] For example, the TQ interface in Thermo-Calc, the "High-throughput calculation" command in PANDAT, and OCASI in OpenCALPHAD can be used for such calculations. To use the thermodynamic data in machine learning, the data have to be digitalized. The digitalized phase diagrams are provided through MatNAVI on the NIMS website.[48] In addition to the phase diagram calculations, there are other useful software packages such as ASCENDS,[46] Extensible Self-optimizing Phase Equilibria Infrastructure (ESPEI),[49] CALTPP,[50] and MatCalc.[51]

3.3. Thermodynamic Database

Various thermodynamic databases have been constructed for each thermodynamic software package.[41] The detailed information on the databases is provided by the developers, where the ranges of the composition, temperature, and pressure are explained. As these commercial databases are encrypted, users cannot read them and see the parameters used in the databases. To solve this problem, open databases were constructed, such as the NIMS computational phase diagram database (CPDDB),[52] NIST database,[53] TAF-ID (project member only),[54] Thermodynamic database database,[55] and OpenCALPHAD database.[43] Moreover, phase diagrams accumulated on the CPDDB are converted into a digital format and provided on Digital-CPDDB.[56] Once phase diagrams are digitalized and stored with thermodynamic quantities, various property values, and metadata, users would be able to search for thermodynamic information instead of calculating them on a special software package.

The final goal of the database construction would be the database for 100 element systems. On the ASM phase diagram database[57] most binary systems have been included, although some of them are still partial phase diagrams. To accelerate the construction and assessment of phase diagrams, first-principles calculations[58–61] have been widely adopted to estimate thermodynamic quantities of stable and metastable states. Moreover, evaluations of phase diagrams[62,63] and efficient construction methods of phase diagrams using uncertainty analysis have been proposed.[64,65]

The Gibbs energy of unary systems is the basis of thermodynamic assessments and databases in the CALPHAD. The lattice stability introduced by Kaufman,[5] the first-generation database, was revised in 1991.[10] This is called the second-generation database, which is available as the SGTE–Pure database and can be downloaded from the SGTE website.[11] This second-generation database has been updated several times with minor modifications. The lower limit of the applicable temperature range of this second-generation database is usually the RT. To expand the temperature range using the Einstein function, the third-generation database is intensively constructed.[66–71]

4. First-principles Calculations

4.1. Outline of First-principles Calculations

The "first-principles calculations" is a technique for calculating various physical properties of a substance, including its energy, using only the atomic number and crystal structure information. Specifically, the total energy of the electron system is expressed in Eq. (4) by the adiabatic approximation,[72] in which the motion of the nucleus is assumed to be sufficiently less than that of the electron to be negligible. Furthermore, the electron density functional theory (DFT)[73,74] treats electrons as electron density:

$$E_{\text{total}}^{\text{elec}}[\rho] = T[\rho] + \int V_{\text{ion}}(r)\rho(r)dr + \frac{e^2}{2}\iint \frac{\rho(r)\rho(r')}{|r-r'|}drdr' + E_{\text{xc}}[\rho], \quad \text{..... (4)}$$

where ρ is the electron density and $E_{\text{total}}^{\text{elec}}[\rho]$ is the energy for the electron density distribution. On the right side of the equation, the first term $T[\rho]$ is the electron's kinetic energy; the second term $V_{\text{ion}}(r)$ is the electrostatic potential from the nucleus acting on the electrons at the coordinate r; and the third term is the classical electrostatic potential between electrons. The fourth term $E_{\text{xc}}[\rho]$ is the exchange correlation energy that includes all the remaining many-body interactions. Because calculating the exact form of the exchange correlation energy analytically is challenging, the local density approximation and the generalized gradient approximation are used in the actual calculations.

The total energy acquired from first-principles calculations can be used to calculate the enthalpy of formation of the compound to be introduced into the CALPHAD method. Equation (5) expresses the enthalpy of formation of a binary compound A_nB_m ($H_{A_nB_m}$):

$$H_{A_nB_m} = E_{A_nB_m} - \left(nE_A + mE_B\right). \quad \text{..... (5)}$$

Here, E_ϕ is the total energy per composition formula of the structure ϕ determined from the first-principles calculation. That is, $E_{A_nB_m}$ is the total energy of the binary compound A_nB_m, where E_A and E_B are the total energies of the simple substance for elements A and B, respectively, before the reaction. To be precise, the PV term is added to the right-hand side of Eq. (5), which can be ignored when the pressure is small, such as at ambient pressure.

4.2. Free Energy Calculation at Finite Temperatures

The energy corresponding to absolute zero is obtained in first-principles calculations by calculating the static electronic state. By contrast, because the state of the free energy minimum is realized in real phase equilibrium, it is important to determine the free energy in the phase diagram calculation using the CALPHAD method. The contribution of the entropy term from the lattice oscillation, atomic configuration, magnetic, and electronic specific heat must be included in the free energy. Each contribution can be calculated using first-principles calculations to derive the interaction between atoms and magnetic spins and the density of states of electrons, and applying statistical and thermodynamic calculations. In addition, because just a few electrons at the Fermi surface contribute to the entropy, the entropy from electrons has a small contribution to the free energy. By contrast, due to the large contribution of the entropy term in the lattice oscillation and atomic configuration, we discuss the calculation method that deals with these in Sections 4.2.1 and 4.2.2. Furthermore, the free energy can be calculated even in the liquid phase by evaluating the enthalpy and entropy of vibration and the configuration of atoms using the first-principles molecular dynamics method, which is described in Section 4.2.3.

4.2.1. Lattice Vibration

The calculation of the quasi-harmonic approximation by phonon calculation, which is a typical calculation method for dealing with lattice vibration, is described here. The restoring atomic force generated by minute displacement of the atomic position from the equilibrium position is evaluated using this method. The wave number dependence of the frequency (ω_V) of the phonon is obtained by calculating the second-order force constants for the atomic displacement from these restoring forces at volume V. This harmonic oscillation approximation is a technique for approximating the force constant of the second order. Helmholtz energy, including the effect of lattice vibration at finite temperatures, is given as Eq. (6) using the wavenumber dependence of phonon frequency:

$$F_V(T) = E_V + \frac{\hbar}{2}\sum_{\boldsymbol{q}_j}\omega_V(\boldsymbol{q}_j) + k_{\mathrm{B}}T\sum_{\boldsymbol{q}_j}\ln\left[1-\exp\left(\frac{-\hbar\omega_V(\boldsymbol{q}_j)}{k_{\mathrm{B}}T}\right)\right], \quad \text{..... (6)}$$

where E_V is the atomic position equilibrium energy at volume V and $\boldsymbol{q}_j$ is the wave vector at the j-th phonon mode. The second term is the zero-point energy derived from the effect that atomic oscillations exist even at absolute zero. Calculating the volume–energy curve from Helmholtz energy (F_V) in several different volumes and obtaining the volume at which the energy is minimized at a constant pressure condition yields the Gibbs energy:

$$G(T) = \min_V\left[F_V(T)+PV\right] \approx \min_V\left[F_V(T)\right]. \quad \text{..... (7)}$$

The right-hand side approximation assumes that the PV term contributor is small enough for F_V and can be ignored and is a valid approximation under normal pressure (P = 10^5 Pa). PHONOPY[75–77] and ALAMODE[78–80] have been published as open-source code to assist with lattice vibration computation.

4.2.2. Free Energy of Mixing

In a multicomponent system, the free energy of mixing needs to be considered in addition to the contribution of lattice vibration. The alloy composition determines the configuration entropy in an ideal solution. By contrast, in a real solid solution, there is entropy deviation from the ideal solution due to the formation of SRO of the solute. The cluster expansion and cluster variation method (CE-CVM) is a typical technique for assessing the effectiveness of SROs. In this method, we focus on the various atomic configurations (clusters) present in solid solutions and determine the energy (effective cluster interactions (ECIs)) of these clusters analytically.

Specifically, by introducing a correlation function $\langle\phi_\alpha\rangle$ that has a one-to-one correspondence with the density of clusters included in the ordered structure, the energy E_R of the ordered structure is expressed by the sum of the product of the correlation function and ECI (e_{null}, e_{point}, e_{pair}, e_{tri},...):

$$E_R = \sum_{\alpha}^{\alpha_{\max}} e_\alpha \cdot \langle\phi_\alpha\rangle. \quad \text{..... (8)}$$

In theory, Eq. (8) can reproduce the energy of strictly ordered structures using an infinite variety of clusters, but in realistic calculations, the number of clusters used needs to be finite.

Setting a threshold for cluster bond length and selecting only clusters that are shorter than the threshold is a typical approach. The threshold that defines the maximum-size cluster is $\alpha_{\max.}$ That is, Eq. (8) calculates the sum of energies of the clusters contained in $\alpha_{\max}$.

The unknowns are only e_α of ECIs because the correlation function $\langle\phi_\alpha\rangle$ is obtained from the ordered structure, and the total energy on the left-hand side is obtained from the first-principles calculations. Therefore, the ECIs are determined using the least squares method, which involves preparing a number of relational expressions for different ordered structures and energies.[81]

Once ECI is determined, the energies of any atomic arrangement can be determined within the accuracy of the cluster expansion without performing first-principles calculations. In addition, in the case of the cluster arrangement, the free energy, including the entropy of the arrangement, can be expressed as follows:

$$F(T) = \sum_{\alpha}^{\alpha_{\max}} e_\alpha \cdot \langle\phi_\alpha\rangle - T\sum_{\alpha}^{\alpha_{\max}} \gamma_\alpha \cdot S_\alpha. \quad \text{..... (9)}$$

The second term's entropy term is added to Eq. (8), which is the contribution of entropy from the cluster α using the Kikuchi–Barker factor $\gamma_\alpha \cdot S_\alpha$.[82] The free energy is calculated by applying the variational method to Eq. (9) and obtaining a correlation function that minimizes the energy. ATAT[83] and CLUPAN[84,85] are published as representative tools to support the CVM. An example of the Fe–Ni phase diagram calculation using CVM is shown in Fig. 5 (Section 3.1.1).

4.2.3. Free Energy Calculation of the Liquid Phase

Because the interatomic force can be calculated using first-principles, molecular dynamics calculations based on this force are possible. This calculation technique is called

the first-principles molecular dynamics method. The vibrations of atoms at finite temperatures, including anharmonic components, can be calculated in this computation, as can the thermodynamic quantities of systems with disordered atomic arrangements, such as liquids.[86] As an example of liquid phase free energy calculation, this section describes an approximate calculation method called the two-phase model.

The density of states at frequency 0 exists, and the vibrational entropy in the liquid phase differs significantly from that in the solid phase. Thus, the calculation of Eq. (6) diverges to infinity, preventing the same calculation method as the solid phase from being performed. A two-phase model that analytically calculates the vibrational entropy of a finite temperature has been devised as one computational method to solve this problem.[87] To avoid energy computation divergence at frequency 0, this model approximates the density of state (D^{l}) of the liquid phase as two components, the solid phase component (D^{s}) and the gas phase component (D^{g}), as shown in Eq. (10):

$$D^{\mathrm{l}}(\omega) = D^{\mathrm{s}}(\omega) + D^{\mathrm{g}}(\omega). \quad \text{..... (10)}$$

The entropy calculation of the rigid sphere fluid is used, assuming that the density of states with frequency 0 is derived from the gas phase. In addition, the entropy of the solid phase component is calculated using Eq. (6) and S^{vib} is calculated as their sum:

$$S^{\mathrm{vib}} = k_{\mathrm{B}} \int \left[D^{\mathrm{s}}(\omega) W^{\mathrm{s}}(\omega) + D^{\mathrm{g}}(\omega) W^{\mathrm{g}}(\omega) \right] d\omega. \quad \text{... (11)}$$

Here, W^{s} and W^{g} are the weighting functions of the solid phase and gas phase components for entropy, respectively.

4.3. Theoretical Phase Diagram

The possibility of a theoretical phase diagram that does not use the experimental value at all is examined from the equilibrium calculation by the free energy value obtained through a series of techniques in Section 4.2.[88–90] In these studies, free energy calculations in those compounds are carried out utilizing known structural databases, and the phase equilibrium is calculated using prior knowledge of possible phases to be equilibrated. By contrast, a computational tool for searching unknown stable and metastable structures from first-principles calculations has recently been developed, and when these computational methods are used together, it is expected to realize the theoretical phase diagram calculation in completely unknown alloy systems.

USPEX[91,92] and XtalOpt,[93,94] based on genetic algorithms, CrySPY,[95,96] based on Bayesian optimization, and CALYPSO,[97,98] based on particle swarm optimization methods, are examples of typical structural search tools. Using genetic algorithms as an example, this section describes the stable structure searching method.[92,99,100] This is a computational technique that mimics Darwin's evolutionary theory by applying natural selection, heredity, and mutants to the crystal structure. The calculations are carried out in the following flow.

(1) The energy of a random set of ordered structures is calculated, and some of the structures with lower energies and some of the unstable structures (natural selection) are left.

(2) The local atomic arrangements of the remaining structures are regarded as genes, and the following operation results in the formation of a new structure group.

(2-1) Keep the same structure (surviving) without modifying the parameters of the stable structure.

(2-2) Combine two stable structural parameters (heredity).

(2-3) Modify a part of the structural parameters of a stable structure using random numbers (mutation).

(3) Energy calculations are performed for a new generation of structures, and low-energy ones are reselected.

The stable structure is then searched by repeatedly executing processes (2) and (3) and updating the low-energy structure group. In addition, the convex hull of the structure group with the lowest energy is composed of the composition–energy points obtained. The vertex structure of the convex hull is the ground structure at absolute zero, and the phase diagram is constructed using first-principles calculations. In addition, the theoretical phase diagram at finite temperatures can be generated by carrying out a free energy calculation at finite temperatures for the ground and the metastable structures with a small energy difference from the ground structures. An example of a phase diagram obtained using this method is presented in **Fig. 7**(a). The phase diagram in Fig. 7(a) differs slightly from that in Fig. 7(b), but the approximate equilibrium is reproduced. In addition, it has been confirmed that the actual phase diagram can be reproduced by only adding an energy correction of

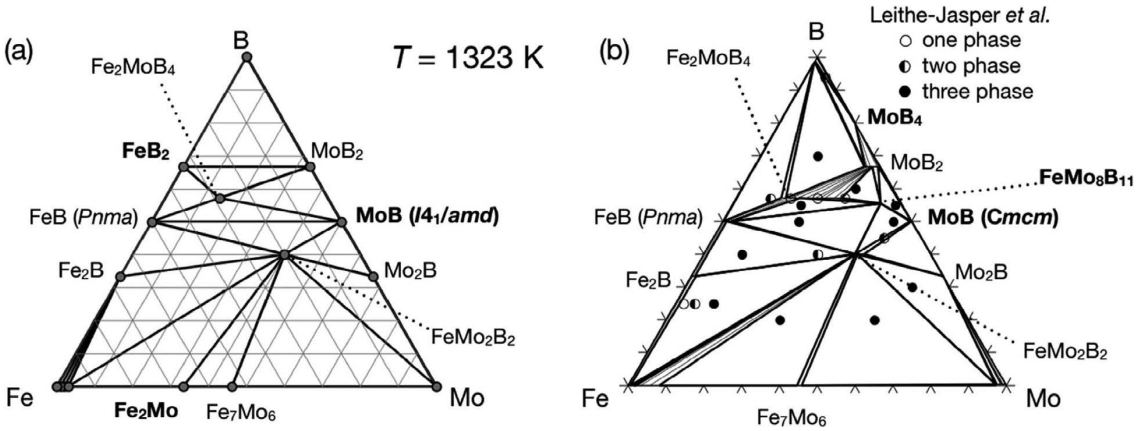

Fig. 7. (a) Theoretical phase diagram of the Fe–Mo–B ternary system at 1 323 K and (b) computational phase diagram using the CALPHAD method.[90]

about 2 kJ/mol, and it is considered that the free energy is nearly equivalent to the actual phase equilibrium.[90] The elimination of this discrepancy will become an issue in the future, and the causes of this discrepancy include the effects of anharmonic components of lattice vibration and magnetic entropy that were not incorporated in the calculations. By contrast, while the theoretical phase diagram is an ideal phase diagram with no impurities, impurities are rarely able to achieve phase equilibrium. In addition, some systems take a long time to reach equilibrium. Therefore, a comparison between the theoretical and experimental phase diagrams is expected to lead to new discoveries.

5. Data Science

5.1. Status of Data-driven Science for Structural Materials

This section describes the trend of data utilization for structural material development, the data-driven approach, data utilization, and the uncertainty in phase diagram research. Although there are many descriptors for explaining the phenomena in structural materials design, significant labor and time are required to acquire one experimental dataset. Therefore, utilization of existing data and efficient data acquisition are required for materials design. Projects for structural materials research include the Integrated Computational Materials Engineering, ICME and the Materials Genome Initiative, MGI, which are directed by the United States.[101,102] Materials design has been explored as a linkage of process–structure–property–performance with a focus on the use of computational science, in which the CALPHAD method plays a central role in linking process and microstructural information, and has been used to boost alloy design and improve processes.[103] In addition, the "Materials Research by Information Integration" initiative[104] for the development of functional materials and the cross-ministerial Strategic Innovation Promotion program[105–107] for the development of structural materials are being executed with the aim of inverse problem analysis to design alloy compositions and processes for the intended performance.

Machine learning and artificial intelligence are often used in the classification and regression of multidimensional data. Various machine learning algorithms were proposed,[108] and they need to be selected according to the quantity of data and the purpose of the analysis.

5.2. Phase Diagram Analysis and Reliability Evaluation by Data-driven Analysis

In recent years, data-driven type of analyses, seeking to summarize phenomena from data, has become popular because the cost of data acquisition has been lowered and data analysis technology has improved.

The accuracy of the experimental data used varies by data, and therefore in thermodynamic analysis an evaluation that includes error is required. The Bayesian inference, in which the probability distribution is renewed from the state when the data are insufficient, is often used in this technique. The model itself has a random variable in Bayesian estimation, and the variable is evaluated from the observed data to obtain an *a posteriori* distribution. When the materials data are always inadequate and it is difficult to create a clear model with respect to the data to be examined, it is valid to refine the probability distribution model while efficiently enhancing the data using Bayesian optimization and active learning. If the parameters related to the thermodynamic model can be captured probabilistically, the effect of the reliability of the experimental data on the model can be evaluated in the phase diagram.

The analytical method that incorporates uncertainty information estimated from experimental data is called CALPHAD UQ.[109,110] It began in 2003 with the study of UO_2–BeO by Stan *et al.*[111] They use a genetic algorithm and Bayesian optimization to assess the uncertainty of phase boundaries, considering the errors in experimentally reported data, as well as the model's reliability. In recent years, the tool called ESPEI[49,112,113] for fitting thermodynamic model parameters and quantifying uncertainties has been created. Model parameters for Gibbs energy in CALPHAD will be generated using tools for data-driven model selection. Then, the Bayesian ensemble Markov chain Monte Carlo method is used to optimize model parameters and uncertainty quantification. The phase diagram in **Fig. 8** was constructed using the Cu–Mg system as an example. Other systems that were assessed for uncertainty were U–Nb,[114] the Ti_2AlC–Cr_2AlC pseudo-binary system,[115] Hf–Si,[116] Hf single phase,[117] and Al–Hf.[118]

Combinatorial methods for obtaining experimental data could be enhanced by active learning. In particular, when the available data for the parameter space are small, it seems important to perform the experiment while balancing the exploration (data acquisition, which contributes to the refinement of the prediction model) and exploitation (data acquisition to obtain the desired performance) of the parameter space utilizing techniques such as active learning.[119,120] A method for determining the phase boundaries in the oxide phase diagram efficiently using the uncertainty sampling (US) method for active learning[121,122] has been proposed. The vicinity of the phase boundary is actively sampled at a point determined to be highly uncertain from the data from established phase diagrams. By evaluating known experimental phase diagrams using this technique, it was shown that the US method can reduce the number of sampling points by about 20% compared with random sampling (**Fig. 9**). It has also been shown that new undetected

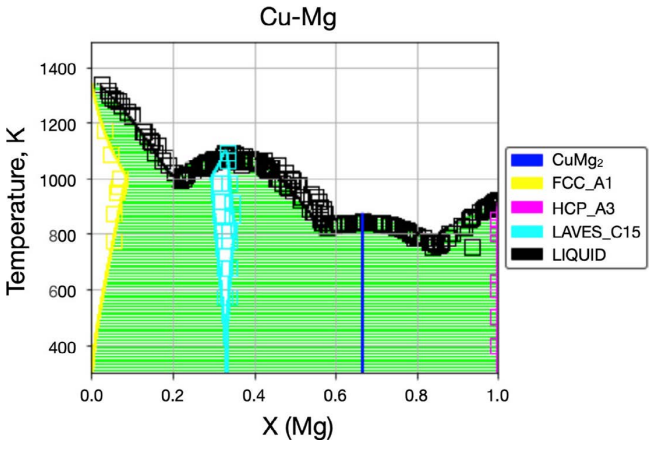

Fig. 8. The Cu–Mg binary phase diagram with parameters refined by Bayesian optimization.[49] (Online version in color.)

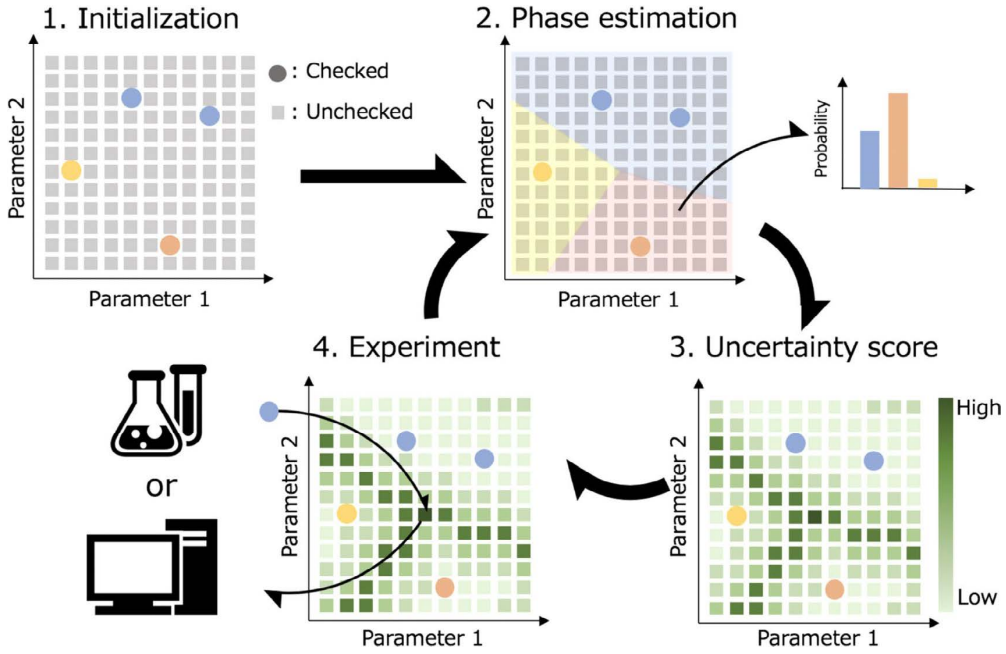

Fig. 9. Refinement process of the oxide phase diagram using active learning.[122] (Online version in color.)

phases can be quickly discovered and that a small number of initial sampling points is sufficient.

5.3. Libraries for Experimental and Computing Databases and Programming

With the progress in data analysis technologies, further data storage and utilization have become necessary, and the construction of databases and data infrastructure (*i.e.*, the basis for handling data) has become more urgent. Recently, more data can be accessed by a database of as many as 1 million DFT calculations via high-throughput DFT.[123–133] Himanen compiled infrastructures and databases related to materials data.[134] In Europe, an analysis environment is being constructed in which various datasets are used in a cross-sectional manner with a focus on the Novel Materials Database.[135] At the same time, Japan is becoming more active in the promotion of data-driven research and the development of materials data platforms.[136] Libraries and platforms[113,128,131,137–139] for analyzing such data have been developed and are becoming powerful tools for the design and development of materials in the future.

6. Conclusions

The phase diagram can provide basic information for microstructural control of various materials; the thermodynamically calculated phase diagram represented by the experimental phase diagram and the CALPHAD method accumulated to date have made significant advances in this field. Furthermore, recent remarkable developments in first-principles calculations and data science technology have increased the accuracy of thermodynamic data and phase equilibrium data predicted by such techniques to an exceedingly high level. This enabled the incorporation of these calculated results as "data with almost the same accuracy as those actually obtained by experiments" into the CALPHAD method, which could not determine the parameters without experimental values. In addition, it is now possible to parameterize not only the stable phase but also the physical properties of thermodynamically unstable phases, and the width of phase equilibrium and dynamic calculations is broadening. The physical properties of such invisible regions are believed to play an even more important role in the future as they form the basis of simulation technology at various levels.

Due to the inclination of universities and research institutes to prohibit dangerous experiments, obtaining experimental values on phase equilibria and thermodynamic properties and analyzing thermodynamic properties as described in Sections 2 and 3 have become harder in recent years. In this regard, new research methods based on first-principles calculations and data science technology described in Sections 4 and 5 will make significant contributions to this field. However, it is also important to remember that the results of these methods are obtained under extremely limited conditions or assumptions. It is the responsibility of the scientists and engineers in the field to discern the meaning and academic significance of these data, as well as the credibility of the new knowledge obtained from them. We hope that the training of material scientists who are well-versed in thermodynamics would receive more emphasis in the higher education in our country.

Acknowledgment

One of the authors (I.O.) wishes to express appreciation to Prof. R. Kainuma for providing his experimental data on DTs. The author (H.O.) gratefully acknowledge the financial support by JSPS KAKENHI (grant numbers, 18H05454 and 21H01602).

REFERENCES

1) Methods for Phase Diagram Determination, ed. by J. C. Zhao, Elsevier, Oxford, UK, (2007), 1. https://doi.org/10.1016/B978-0-08-044629-5.X5000-9
2) I. Ohnuma, S. Shimenouchi, T. Omori, K. Ishida and R. Kainuma: *Calphad*, **67** (2019), 101677. https://doi.org/10.1016/j.calphad.2019.101677

3) T. Miyamoto, M. Nagasako and R. Kainuma: *J. Alloy. Compd.*, **549** (2013), 57. https://doi.org/10.1016/j.jallcom.2012.08.128
4) T. Nishizawa: Thermodynamics of Microstructures, ASM International, Materials Park, OH, (2008), 1.
5) L. Kaufman and H. Bernstein: Computer Calculation of Phase Diagrams, Academic Press, New York, (1970), 1.
6) M. Hillert: Phase Equilibria, Phase Diagrams and Phase Transformations, Cambridge University Press, Cambridge, UK, (1998), 1.
7) N. Saunders and A. P. Miodownik: CALPHAD–Calculation of Phase Diagrams, A Comprehensive Guide, Elsevier, Amsterdam, (1998), 1.
8) J. J. van Laar: *Z. Phys. Chem.*, **63U** (1908), 216. https://doi.org/10.1515/zpch-1908-6314
9) E. A. Guggenheim: Mixtures, Clarendon Press, Oxford, UK, (1952), 1.
10) A. T. Dinsdale: *Calphad*, **15** (1991), 317. https://doi.org/10.1016/0364-5916(91)90030-N
11) SGTE-database, SGTE, Grenoble, (2009).
12) W. L. Bragg and E. J. Williams: *Proc. R. Soc. Lond. A*, **145** (1934), 699. https://doi.org/10.1098/rspa.1934.0132
13) O. Redlich and A. T. Kister: *J. Chem. Phys.*, **15** (1947), 849. https://doi.org/10.1063/1.1746359
14) A. Janz and R. Schmid-Fetzer: *Calphad*, **29** (2005), 37. https://doi.org/10.1016/j.calphad.2005.01.003
15) M. Hillert and L.-I. Staffansson: *Acta Chem. Scand.*, **24** (1970), 3618. https://doi.org/10.3891/acta.chem.scand.24-3618
16) B. Sundman and J. Ågren: *J. Phys. Chem. Solids*, **42** (1981), 297. https://doi.org/10.1016/0022-3697(81)90144-X
17) A. D. Pelton and P. Chartrand: *Metall. Mater. Trans. A*, **32** (2001), 1355. https://doi.org/10.1007/s11661-001-0226-3
18) B. Predel, M. Hoch and M. Pool: Phase Diagrams and Heterogeneous Equilibria, A Practical Introduction, Springer, New York, (2004), 1.
19) B. Sundman: *Calphad*, **15** (1991), 109. https://doi.org/10.1016/0364-5916(91)90010-H
20) P. J. Flory: *J. Chem. Phys.*, **9** (1941), 660. https://doi.org/10.1063/1.1750971
21) M. L. Huggins: *J. Chem. Phys.*, **46** (1942), 151. https://doi.org/10.1021/j150415a018
22) R. Kikuchi: *J. Chem. Phys.*, **60** (1974), 1071. https://doi.org/10.1063/1.1681115
23) M. Enoki, B. Sundman, M. H. F. Sluiter, M. Selleby and H. Ohtani: *Metals*, **10** (2020), 998. https://doi.org/10.3390/met10080998
24) B. Sundman, S. G. Fries and W. A. Oates: *Calphad*, **22** (1998), 335. https://doi.org/10.1016/S0364-5916(98)00034-0
25) T. Abe and B. Sundman: *Calphad*, **27** (2003), 403. https://doi.org/10.1016/j.calphad.2004.01.005
26) T. Abe and M. Shimono: *Calphad*, **45** (2014), 40. https://doi.org/10.1016/j.calphad.2013.11.006
27) T. Abe: *Mater. Trans.*, **62** (2021), 711. https://doi.org/10.2320/matertrans.MT-M2021022
28) G. Inden: *Z. Metallkd.*, **66** (1975), 577. https://doi.org/10.1515/ijmr-1975-661003
29) M. Hillert and M. Jarl: *Calphad*, **2** (1978), 227. https://doi.org/10.1016/0364-5916(78)90011-1
30) Q. Chen and B. Sundman: *J. Phase Equilib.*, **22** (2001), 631. https://doi.org/10.1007/s11669-001-0027-9
31) W. Xiong, Q. Chen, P. A. Korzhavyi and M. Selleby: *Calphad*, **39** (2012), 11. https://doi.org/10.1016/j.calphad.2012.07.002
32) P. Franke: *J. Phase Equilib. Diffus.*, **35** (2014), 780. https://doi.org/10.1007/s11669-014-0348-0
33) J. Ågren and M. Hillert: *Calphad*, **67** (2019), 101666. https://doi.org/10.1016/j.calphad.2019.101666
34) T. Abe, M. Shimono, K. Hashimoto and C. Kocer: *Calphad*, **63** (2018), 100. https://doi.org/10.1016/j.calphad.2018.08.010
35) G. Shao: *J. Appl. Phys.*, **88** (2000), 4443. https://doi.org/10.1063/1.1289788
36) X. G. Lu, M. Selleby and B. Sundman: *Calphad*, **29** (2005), 49. https://doi.org/10.1016/j.calphad.2005.04.001
37) CaTCalc, Research Institute of Computational Thermodynamics, Saga, (2022).
38) Malt2 for windows, Malt group, Tokyo, (2004).
39) PANDAT, CompuTherm LLC, Middleton, WI, (2022).
40) FactSage, GTT-Technologies, Herzogenrath, (2022).
41) Thermo-Calc, Thermo-Calc Software, Solna, (2022).
42) H. L. Lukas, H. T. Henig and B. Zimmermann: *Calphad*, **1** (1977), 225.
43) OpenCalphad, Interdisciplinary Centre for Advanced Materials Simulations, Bochum, (2015).
44) pycalphad, pycalphad Development Team, Pennsylvania, (2015).
45) R. Shi, D. Chandra, W. M. Chien and J. Wang: *Calphad*, **64** (2019), 66. https://doi.org/10.1016/j.calphad.2018.11.005
46) J. Peng, E. Lara-Curzio and D. Shin: *Calphad*, **66** (2019), 101631. https://doi.org/10.1016/j.calphad.2019.101631
47) S. Samanta and A. van de Walle: *Calphad*, **74** (2021), 102306. https://doi.org/10.1016/j.calphad.2021.102306
48) NIMS DigiPD System, NIMS, Ibaraki, (2021). https://doi.org/10.48505/nims.3061
49) ESPEI, Materials Genome Foundation, Pennsylvania, (2018).
50) S. Wen, Y. Liu, H. Liu, Q. Min, Y. Du, C. Du, Z. Zheng, P. Zhou, S. Zhang and M. Chu: *Calphad*, **72** (2021), 102229. https://doi.org/10.1016/j.calphad.2020.102229
51) MatCalc, MatCalc Engineering, Vienna, (2009).
52) NIMS CPDDB Computational Phase Diagram Database, NIMS, Ibaraki, (2016). https://doi.org/10.48505/nims.3060
53) NIST Materials Data Repository, NIST, Gaithersburg, MD.
54) C. Guéneau, N. Dupin, L. Kjellqvist, E. Geiger, M. Kurata, S. Gossé, E. Corcoran, A. Quaini, R. Hania, A. L. Smith, M. H. A. Piro, T. Besmann, P. E. A. Turchi, J. C. Dumas, M. J. Welland, *et al.*: *Calphad*, **72** (2021), 102212. https://doi.org/10.1016/j.calphad.2020.102212
55) A. van de Walle, C. Nataraj and Z.-K. Liu: *Calphad*, **61** (2018), 173. https://doi.org/10.1016/j.calphad.2018.04.003
56) NIMS Digital-CPDDB, NIMS, Ibaraki, (2021).
57) ASM Alloy Phase Diagram Database, ASM Phase Diagram Center, Ohio, (2012).
58) T. Davey, N. D. Tran, A. Saengdeejing and Y. Chen: *Calphad*, **71** (2020), 102008. https://doi.org/10.1016/j.calphad.2020.102008
59) S. Tumminello, M. Palumbo, J. Koßmann, T. Hammerschmidt, P. R. Alonso, S. Sommadossi and S. G. Fries: *Metals*, **10** (2020), 1142. https://doi.org/10.3390/met10091142
60) M. Enoki and H. Ohtani: Encyclopedia of Materials: Metals and Alloys, Vol. 2, Elsevier, Amsterdam, (2022), 284. https://doi.org/10.1016/B978-0-12-819726-4.00032-6
61) M. Enoki, K. Takahashi, S. Mitomi and H. Ohtani: *ISIJ Int.*, **60** (2020), 2963. https://doi.org/10.2355/isijinternational.ISIJINT-2020-189
62) M. Palumbo, S. G. Fries, A. Dal Corso, F. Körmann, T. Hickel and J. Neugebauer: *J. Phys. Condens. Matter*, **26** (2014), 335401. https://doi.org/10.1088/0953-8984/26/33/335401
63) A. van de Walle and Q. Hong: *J. Phase Equilib. Diffus.*, **40** (2019), 170. https://doi.org/10.1007/s11669-019-00711-5
64) K. Terayama, R. Tamura, Y. Nose, H. Hiramatsu, H. Hosono, Y. Okuno and K. Tsuda: *Phys. Rev. Mater.*, **3** (2019), 033802. https://doi.org/10.1103/PhysRevMaterials.3.033802
65) K. Tsutsui and K. Moriguchi: *Calphad*, **74** (2021), 102303. https://doi.org/10.1016/j.calphad.2021.102303
66) B. Sundman, U. R. Kattner, M. Hillert, M. Selleby, J. Ågren, S. Bigdeli, Q. Chen, A. Dinsdale, B. Hallstedt, A. Khvan, H. Mao and R. Otis: *Calphad*, **68** (2020), 101737. https://doi.org/10.1016/j.calphad.2020.101737
67) A. V. Khvan, I. A. Uspenskaya, N. M. Aristova, Q. Chen, G. Trimarchi, N. M. Konstantinova and A. D. Dinsdale: *Calphad*, **68** (2020), 101724. https://doi.org/10.1016/j.calphad.2019.101724
68) A. Bigdeli, L. F. Zhu, A. Glensk, B. Grabowski, B. Lindahl, T. Hickel and M. Selleby: *Calphad*, **65** (2019), 79. https://doi.org/10.1016/j.calphad.2019.02.008
69) B. Hu, S. Sridar, L. Hao and W. Xiong: *Intermetallics*, **122** (2020), 106791. https://doi.org/10.1016/j.intermet.2020.106791
70) Z. He, B. Kaplan, H. Mao and M. Selleby: *Calphad*, **72** (2021), 102250. https://doi.org/10.1016/j.calphad.2021.102250
71) G. Deffrennes, N. Jakse, C. M. S. Alvares, I. Nuta, A. Pasturel, A. Khvan and A. Pisch: *Calphad*, **69** (2020), 101764. https://doi.org/10.1016/j.calphad.2020.101764
72) M. Born and R. Oppenheimer: *Ann. Phys.*, **389** (1927), 457.
73) P. Hohenberg and W. Kohn: *Phys. Rev.*, **136** (1964), B864. https://doi.org/10.1103/physrev.136.b864
74) W. Kohn and L. J. Sham: *Phys. Rev.*, **140** (1965), A1133. https://doi.org/10.1103/physrev.140.a1133
75) A. Togo, F. Oba and I. Tanaka: *Phys. Rev. B*, **78** (2008), 134106. https://doi.org/10.1103/PhysRevB.78.134106
76) A. Togo, L. Chaput, I. Tanaka and G. Hug: *Phys. Rev. B*, **81** (2010), 174301. https://doi.org/10.1103/PhysRevB.81.174301
77) PHONOPY, A. Togo, Kyoto, (2009).
78) T. Tadano, Y. Gohda and S. Tsuneyuki: *J. Phys. Condens. Matter*, **26** (2014), 225402. https://doi.org/10.1088/0953-8984/26/22/225402
79) T. Tadano and S. Tsuneyuki: *Phys. Rev. B*, **92** (2015), 054301. https://doi.org/10.1103/PhysRevB.92.054301
80) ALAMODE, T. Tadano, Tsukuba, (2014).
81) M. H. F. Sluiter, C. Colinet and A. Pasturel: *Phys. Rev. B*, **73** (2006), 174204. https://doi.org/10.1103/PhysRevB.73.174204
82) R. Kikuchi: *Phys. Rev.*, **81** (1951), 988. https://doi.org/10.1103/PhysRev.81.988
83) Alloy Theoretic Automated Toolkit (ATAT), A. van de Walle, Rhode Island, (2002).
84) CLUPAN, A. Seko, Kyoto, (2010).
85) A. Seko, Y. Koyama and I. Tanaka: *Phys. Rev. B*, **80** (2009), 165122. https://doi.org/10.1103/PhysRevB.80.165122
86) L. F. Zhu, B. Grabowski and J. Neugebauer: *Phys. Rev. B*, **96** (2017), 224202. https://doi.org/10.1103/PhysRevB.96.224202
87) S.-T. Lin, M. Blanco and W. A. Goddard III: *J. Chem. Phys.*, **119**

(2003), 11792. https://doi.org/10.1063/1.1624057
88) A. van de Walle, R. Sun, Q. J. Hong and S. Kadkhodaei: *Calphad*, **58** (2017), 70. https://doi.org/10.1016/j.calphad.2017.05.005
89) T. Davey, N. D. Tran, A. Saengdeejing and Y. Chen: *Calphad*, **71** (2020), 102008. https://doi.org/10.1016/j.calphad.2020.102008
90) M. Enoki, K. Takahashi, S. Mitomi and H. Ohtani: *ISIJ Int.*, **60** (2020), 2963. https://doi.org/10.2355/isijinternational.ISIJINT-2020-189
91) USPEX, A. R. Oganov, Moscow, (2012).
92) A. R. Oganov and C. W. Glass: *J. Chem. Phys.*, **124** (2006), 244704. https://doi.org/10.1063/1.2210932
93) XtalOpt, E. Zurek, New York, (2011).
94) Z. Falls, P. Avery, X. Wang, K. P. Hilleke and E. Zurek: *J. Phys. Chem. C*, **125** (2021), 1601. https://doi.org/10.1021/acs.jpcc.0c09531
95) CrySPY, CrySPY Development Team, Nagaoka, (2018).
96) T. Yamashita, S. Kanehira, N. Sato, H. Kino, K. Terayama, H. Sawahata, T. Sato, F. Utsuno, K. Tsuda, T. Miyake and T. Oguchi: *Sci. Technol. Adv. Mater.*, **1** (2021), 87. https://doi.org/10.1080/27660400.2021.1943171
97) CALYPSO, CALYPSO Developers Group, Jilin, (2009).
98) Q. Li, D. Zhou, W. Zheng, Y. Ma and C. Chen: *Phys. Rev. Lett.*, **110** (2013), 136403. https://doi.org/10.1103/PhysRevLett.110.136403
99) A. R. Oganov, A. O. Lyakhov and M. Valle: *Acc. Chem. Res.*, **44** (2011), 227. https://doi.org/10.1021/ar1001318
100) A. O. Lyakhov, A. R. Oganov, H. T. Stokes and Q. Zhu: *Comput. Phys. Commun.*, **184** (2013), 1172. https://doi.org/10.1016/j.cpc.2012.12.009
101) G. B. Olson and C. J. Kuehmann: *Scr. Mater.*, **70** (2014), 25. https://doi.org/10.1016/j.scriptamat.2013.08.032
102) M. F. Horstemeyer: Integrated Computational Materials Engineering (ICME) for Metals, John Wiley and Sons, Hoboken, NJ, (2012), 1. https://doi.org/10.1002/9781118342664.ch1
103) W. Xiong: *JOM*, **67** (2015), 1864. https://doi.org/10.1007/s11837-015-1514-5
104) Material Research by Information Integration Initiative (MI2I), NIMS, Tsukuba, (2015).
105) M. Demura and T. Koseki: *Mater. Trans.*, **61** (2020), 2041. https://doi.org/10.2320/matertrans.MT-MA2020003
106) S. Minamoto, T. Kadohira, K. Ito and M. Watanabe: *Mater. Trans.*, **61** (2020), 2067. https://doi.org/10.2320/matertrans.MT-MA2020002
107) M. Enoki: *Mater. Trans.*, **61** (2020), 2052. https://doi.org/10.2320/matertrans.MT-MA2020007
108) J. Schmidt, M. R. G. Marques, S. Botti and M. A. L. Marques: *npj Comput. Mater.*, **5** (2019), 83. https://doi.org/10.1038/s41524-019-0221-0
109) P. Honarmandi, N. H. Paulson, R. Arróyave and M. Stan: *Model. Simul. Mater. Sci. Eng.*, **27** (2019), 034003. https://doi.org/10.1088/1361-651x/ab08c3
110) P. Honarmandi and R. Arróyave: *Integr. Mater. Manuf. Innov.*, **9** (2020), 103. https://doi.org/10.1007/s40192-020-00168-2
111) M. Stan and B. J. Reardon: *Calphad*, **27** (2003), 319. https://doi.org/10.1016/j.calphad.2003.11.002
112) B. Bocklund, R. Otis, A. Egorov, A. Obaied, I. Roslyakova and Z.-K. Liu: *MRS Commun.*, **9** (2019), 618. https://doi.org/10.1557/mrc.2019.59
113) N. H. Paulson, B. J. Bocklund, R. A. Otis, Z.-K. Liu and M. Stan: *Acta Mater.*, **174** (2019), 9. https://doi.org/10.1016/j.actamat.2019.05.017
114) T. C. Duong, R. E. Hackenberg, A. Landa, P. Honarmandi, A. Talapatra, H. M. Volz, A. Llobet, A. I. Smith, G. King, S. Bajaj, A. Ruban, L. Vitos, P. E. A. Turchi and R. Arróyave: *Calphad*, **55** (2016), 219. https://doi.org/10.1016/j.calphad.2016.09.006
115) T. C. Duong, A. Talapatra, W. Son, M. Radovic and R. Arróyave: *Sci. Rep.*, **7** (2017), 5138. https://doi.org/10.1038/s41598-017-05463-1
116) P. Honarmandi, T. C. Duong, S. F. Ghoreishi, D. Allaire and R. Arroyave: *Acta Mater.*, **164** (2019), 636. https://doi.org/10.1016/j.actamat.2018.11.007
117) N. H. Paulson, E. Jennings and M. Stan: *Int. J. Eng. Sci.*, **142** (2019), 74. https://doi.org/10.1016/j.ijengsci.2019.05.011
118) N. H. Paulson, S. Zomorodpoosh, I. Roslyakova and M. Stan: *Calphad*, **68** (2020), 101728. https://doi.org/10.1016/j.calphad.2019.101728
119) M. L. Green, C. L. Choi, J. R. Hattrick-Simpers, A. M. Joshi, I. Takeuchi, S. C. Barron, E. Campo, T. Chiang, S. Empedocles, J. M. Gregoire, A. G. Kusne, J. Martin, A. Mehta, K. Persson, Z. Trautt, J. Van Duren and A. Zakutayev: *Appl. Phys. Rev.*, **4** (2017), 011105. https://doi.org/10.1063/1.4977487
120) K. S. Vecchio, O. F. Dippo, K. R. Kaufmann and X. Liu: *Acta Mater.*, **221** (2021), 117352. https://doi.org/10.1016/j.actamat.2021.117352
121) C. Dai and S. C. Glotzer: *J. Phys. Chem. B*, **124** (2020), 1275. https://doi.org/10.1021/acs.jpcb.9b09202
122) K. Terayama, R. Tamura, Y. Nose, H. Hiramatsu, H. Hosono, Y. Okuno and K. Tsuda: *Phys. Rev. Mater.*, **3** (2019), 033802. https://doi.org/10.1103/PhysRevMaterials.3.033802
123) S. Kirklin, J. E. Saal, B. Meredig, A. Thompson, J. W. Doak, M. Aykol, S. Rühl and C. Wolverton: *npj Comput. Mater.*, **1** (2015), 15010. https://doi.org/10.1038/npjcompumats.2015.10
124) S. Curtarolo, W. Setyawan, S. Wang, J. Xue, K. Yang, R. H. Taylor, L. J. Nelson, G. L. W. Hart, S. Sanvito, M. Buongiorno-Nardelli, N. Mingo and O. Levy: *Comput. Mater. Sci.*, **58** (2012), 227. https://doi.org/10.1016/j.commatsci.2012.02.002
125) A. Jain, S. P. Ong, G. Hautier, W. Chen, W. D. Richards, S. Dacek, S. Cholia, D. Gunter, D. Skinner, G. Ceder and K. Persson: *APL Mater.*, **1** (2013), 011002. https://doi.org/10.1063/1.4812323
126) L. Ward, A. Dunn, A. Faghaninia, N. E. R. Zimmermann, S. Bajaj, Q. Wang, J. Montoya, J. Chen, K. Bystrom, M. Dylla, K. Chard, M. Asta, K. A. Persson, G. J. Snyder, I. Foster and A. Jain: *Comput. Mater. Sci.*, **152** (2018), 60. https://doi.org/10.1016/j.commatsci.2018.05.018
127) K. Mathew, J. H. Montoya, A. Faghaninia, S. Dwarakanath, M. Aykol, H. Tang, I. h. Chu, T. Smidt, B. Bocklund, M. Horton, J. Dagdelen, B. Wood, Z.-K. Liu, J. Neaton, S. P. Ong, K. Persson and A. Jain: *Comput. Mater. Sci.*, **139** (2017), 140. https://doi.org/10.1016/j.commatsci.2017.07.030
128) J. Janssen, S. Surendralal, Y. Lysogorskiy, M. Todorova, T. Hickel, R. Drautz and J. Neugebauer: *Comput. Mater. Sci.*, **163** (2019), 24. https://doi.org/10.1016/j.commatsci.2018.07.043
129) E. Martínez-Sancho, L. Slámová, S. Morganti, C. Grefen, B. Carvalho, B. Dauphin, C. Rellstab, F. Gugerli, L. Opgenoorth, K. Heer, F. Knutzen, G. von Arx, F. Valladares, S. Cavers, B. Fady, *et al.*: *Sci. Data*, **7** (2020), 1. https://doi.org/10.1038/s41597-019-0340-y
130) E. B. Tadmor, R. S. Elliott, J. P. Sethna, R. E. Miller and C. A. Becker: *JOM*, **63** (2011), 17. https://doi.org/10.1007/s11837-011-0102-6
131) C. W. Andersen, R. Armiento, E. Blokhin, G. J. Conduit, S. Dwaraknath, M. L. Evans, Á. Fekete, A. Gopakumar, S. Gražulis, A. Merkys, F. Mohamed, C. Oses, G. Pizzi, G. M. Rignanese, *et al.*: *Sci. Data*, **8** (2021), 217. https://doi.org/10.1038/s41597-021-00974-z
132) S. Gražulis, D. Chateigner, R. T. Downs, A. F. T. Yokochi, M. Quirós, L. Lutterotti, E. Manakova, J. Butkus, P. Moeck and A. Le Bail: *J. Appl. Crystallogr.*, **42** (2009), 726. https://doi.org/10.1107/S0021889809016690
133) NOMAD, The Novel Materials Discovery (NOMAD) Laboratory, Berlin, (2018).
134) L. Himanen, A. Geurts, A. S. Foster and P. Rinke: *Adv. Sci.*, **6** (2019), 1900808. https://doi.org/10.1002/advs.201900808
135) C. Draxl and M. Scheffler: *J. Phys. Mater.*, **2** (2019), 036001. https://doi.org/10.1088/2515-7639/ab13bb
136) M. Demura: *J. Inf. Sci. Technol. Assoc.*, **71** (2021), 252 (in Japanese). https://doi.org/10.18919/jkg.71.6_252
137) T. Ueno, T. D. Rhone, Z. Hou, T. Mizoguchi and K. Tsuda: *Mater. Discov.*, **4** (2016), 18. https://doi.org/10.1016/j.md.2016.04.001
138) R. Couperthwaite, A. Molkeri, D. Khatamsaz, A. Srivastava, D. Allaire and R. Arròyave: *JOM*, **72** (2020), 4431. https://doi.org/10.1007/s11837-020-04396-x
139) S. Lee, J. Peng, A. Williams and D. Shin: *J. Open Source Softw.*, **5** (2020), 1656. https://doi.org/10.21105/joss.01656